Articles in PresS. J Neurophysiol (April 8, 2015). doi:10.1152/jn.00179.2015
JN-00179-2015 revised; 4 April 2015

# Deflection of a vibrissa leads to a gradient of strain across mechanoreceptors in a mystacial follicle

Samuel J. Whiteley[1,2], Per M. Knutsen[2,*], David W. Matthews[2] and David Kleinfeld[2,3,*]

[1] Department of Physics, University of Chicago, Chicago, IL 60637
[2] Department of Physics, UC San Diego, La Jolla, CA 92093
[3] Section of Neurobiology, UC San Diego, La Jolla, CA 92093

Abbreviated title: The strain of deflection

Number of pages in submission:

| | |
|---|---|
| Abstract | 191 words |
| Main text | 4430 words |
| Figures: | 4 (all in color) |

Keywords: Biomechanics, displacement, Merkel cells, ringwulst, somatosensation, whisker

*Correspondence:

Prof. David Kleinfeld
Department of Physics 0374
University of California
9500 Gilman Drive
La Jolla, CA 92093
Email: dk@physics.ucsd.edu

Dr. Per M Knutsen
Department of Physics 0374
University of California
9500 Gilman Drive
La Jolla, CA 92093
Email: pknutsen@physics.ucsd.edu

## Abstract

**Rodents use their vibrissae to detect and discriminate tactile features during active exploration. The site of mechanical transduction in the vibrissa sensorimotor system is the follicle sinus complex and its associated vibrissa. We study the mechanics within the ring sinus of the follicle in an *ex vivo* preparation of the mouse mystacial pad. The sinus region has a relatively dense representation of Merkel mechanoreceptors and longitudinal lanceolate endings. Two-photon laser scanning microscopy was used to visualize labeled cell nuclei in an approximately 100 nL volume before and after passive deflection of a vibrissa, which results in localized displacements of the mechanoreceptor cells primarily in the radial and polar directions about the vibrissa. These displacements are used to compute the strain field across the follicle in response to the deflection. We observe compression in the lower region of the ring sinus while dilation, with lower magnitude, occurs in the upper region, with strain $\Delta V/V \sim 0.01$ for a 10° deflection. The extrapolated strain for a 0.1° deflection, the minimum angle that is reported to initiate a spike by primary neurons, corresponds to the minimum strain that activates Piezo2 mechanoreceptor channels.**


**Abbreviations (not to be published)**

| | |
|---|---|
| CS | Cavernous sinus |
| DVN | Deep vibrissa nerve |
| HB | Hair bulb |
| HP | Hair papilla |
| ICB | Inner conical body |
| IM | Mystacial intrinsic muscle |
| IRS | Inner root sheath |
| MDR | Merkel cell dense region |
| MS | Mesenchymal sheath |
| OCB | Outer conical body |
| ORS | Outer root sheath |
| RRC | Rete ridge collar |
| RS | Ring sinus |
| RW | Ringwulst |
| SVN | Superficial vibrissa nerve |
| VS | Vibrissa shaft |

## Introduction

Rodents have set of long flexible hairs, known as macrovibrissae or whiskers, that are arranged as Manhattan-style grids on both sides of their face. The vibrissae serve to detect and potentially recognize objects near the face of the animal. Each vibrissa is held in a follicle-sinus complex and, during contact, the actively applied forces cause the vibrissa shaft to bend (Hires et al., 2013; Quist and Hartmann, 2012). The change in curvature and the obstruction of a vibrissa from its intended angular path are invariant with respect to the latitudinal location of objects (Bagdasarian et al., 2013; O'Connor et al., 2010). The vibrissa-follicle junction is rigid *in vivo* (Bagdasarian et al., 2013), so all mechanical signals are transduced into neuronal signals within the follicle and, to a lesser extent, the surrounding skin (Ebara et al., 2002; Rice et al., 1986; Rice and Munger, 1986). A minimum requirement to decipher the exquisitely sensitive relation between mechanical forces and outputs from primary sensory neurons (Jones et al., 2004) is a model of mechano-electrical transduction within the follicle (Mitchinson et al., 2004).

Transduction of forces into electrical signals is initiated by Merkel cells, which are associated with slowly adapting Aβ afferents (Abraira and Ginty, 2013; Li et al., 2011; Woodbury and Koerber, 2007). Functionally, these afferents encode deflection amplitude and velocity, respond selectively to the direction of deflection (Lichtenstein et al., 1990; Shoykhet et al., 2000), and play an essential role during active touch (Szwed et al., 2003). The functional responses are likely to be molded by the geometry of Merkel cell dense regions and the orientation of afferent endings within the follicle (Ebara et al., 2002; Ikeda and Gu, 2014; Johnson, 2001; Mitchinson et al., 2008; Mitchinson et al., 2004; Rice et al., 1986). Here, we directly measure deformation within the Merkel cell dense region of the follicle that results from passive vibrissae displacements in an *ex vivo* preparation. The deformation is used to compute the volumetric strain, which provides the scale between motion of the vibrissa and distortions of the Merkel dense region of the follicle that can activate mechanosensitive ion channels.

# Methods

Analysis of seven follicles extracted from seven different mice are reported here, of which six were extracted from left side mystacial pads and one from the right side. Another twenty-one follicles were used for establishing micro-dissection and imaging procedures, or were not further analyzed as a result of tissue damage or imaging artifacts. Animal care and treatment conformed to the National Institutes of Health Guidelines and were approved by the Institutional Animal Care and Use Committee at the University of California, San Diego.

*Follicle extraction*

Adult C57BL/6 mice were euthanized by intraperitoneal (IP) injection of 0.1 to 0.2 mL of pentobarbital (Fatal Plus), immediately followed by removal of both mystacial pads. The pads were then further dissected in cold carbogen-infused artificial cerebrospinal fluid (aCSF) (Kleinfeld and Delaney, 1996). A single row of follicles, typically the left C-row, was extracted and then pinned, dorsal side up, on both ends onto a silicone base in an aCSF filled petri dish (**Fig. 1d**). Muscle and other tissue was removed dorsal to a single follicle, typically C1, and an area ~ 1x1 $mm^2$ was exposed at the level of the ring sinus (**Fig. 1e**). Extreme care was exercised to avoid damage to the internal mesenchymal and root sheaths (**Fig. 1f, g**). Blood in the ring sinus was washed out and replaced by aCSF. Regions medial, *i.e.*, cavernous sinus, and lateral, *i.e.*, conical bodies, were not exposed. Throughout the experiment, fresh aCSF at room temperature and bubbled with 95 % $O_2$ and 5 % $CO_2$ was constantly perfused into the imaging dish and across the row of follicles at a rate of 0.03 mL/s.

*Histological labeling of mechanoreceptors*

We examined the distribution of mechanoreceptor types in transgenic mouse that express fluorescent proteins in sensory nerve endings in order to compare the gross features of the mouse follicle with those of other species (Ebara et al., 2002; Rice et al., 1986). *Advillin*$^{Cre/+}$ knockin mice were crossed with red fluorescent protein reporter mice (Ai14) (Madisen et al., 2010) to generate a mouse line that selectively labeled Merkel cells. These are located in the outer root sheath of the follicle at the level of the ring sinus (da Silva et al., 2011). Additionally, we examined the endings that terminate on Merkel cells, as well as lanceolate endings, that terminate in the mesenchymal sheath that is located around the perimeter of the follicle within mice that expressed XFP; expression was incidental to expression of the calcium sensor TN-XXL under the Thy1 promoter (Mank et al., 2008).

Mice were deeply anesthetized with inhalation of 3 to 4 % (v/v) isoflurane in $O_2$, followed

by intraperitoneal injection of 100 to 200 µL pentobarbital (Fatal Plus), transcardially perfused with phosphate-buffered saline followed by fixation in 4 % (w/v) paraformaldehyde in phosphate-buffered saline (PBS) (P3813; Sigma) pH 7.4. After removal from the skull and at least three hours of additional fixation, the mystacial pads were cryoprotected in 30 % (w/v) sucrose in PBS, cut in 60 µm sections on a freezing microtome, and then counterstained with the blue fluorescent nuclear dye DAPI (1:1000; D9542; Sigma-Aldrich).

*Large-scale deformation of a vibrissa*

In a set of experiments to evaluate vibrissa flexion, a separate set of adult C57BL/6 mice were perfused while all vibrissae on the excised pad were statically deflected in the rostral or caudal directions. These excised follicles were stained with the fluorescently-tagged lipophilic dye, 5-hexadecanoylamino-fluorescein, which labels cell membranes (H-110; Invitrogen). Confocal imaging was performed on an Olympus FV1000 confocal microscope and a Leica SP5 upright microscope, using 20X magnification, 100X oil immersion, and 63X glycerol immersion objectives. Images were converted and leveled with the Fiji image processing software.

*Two-photon imaging*

Cell nuclei throughout the dissected tissue were labeled with the blue fluorescent dye DAPI during micro-dissection and transferred to a two-photon laser scanning microscope (TPLSM) for fluorescence imaging at an excitation wavelength of 800 nm. The microscope objective was positioned over the micro-dissected window, which included a region of the ring sinus that extended from the level of the ringwulst out to the medial-aspect of the inner conical body (**Fig. 1e**). For each experimental vibrissae deflection, we scanned a 512×512×180 pixel Z-stack at a resolution of 1 µm/pixel in X and Y and 1.875 µm/pixel in Z, for a 512×512×338 $\mu m^3$ ~ 90 nL volume. Each image stack required ~ 10 minutes of acquisition time. A single experiment included 6 to 24 image stacks.

*Vibrissa deflections*

The vibrissa emerging from the micro-dissected follicle was cut to 30 % of its original length and inserted 100 µm into a glass pipette that was coupled to a micrometer-resolution manipulator (**Fig. 1d**) (MPC- 200; Sutter Instrument). The average distance of the glass pipette mouth to the vibrissa-follicle junction was 7 ± 2 mm, a distance at which the vibrissa is rigid and thus the axial force during deflections minimal (Quist and Hartmann, 2012). The vibrissa was deflected a distance corresponding to either 10° or 20° of angle at the base, in either the rostral (forward) or caudal (backward) direction. The vibrissa remained in the deflected position while a two-photon

image stack was acquired. Each deflection was followed by a return to the rest angle, which was also imaged for comparison and calculation of relative displacements. Each deflection condition was repeated 3 to 12 times on a single follicle.

*Data analysis*

Relative displacements of DAPI labeled cell nuclei were estimated by computing rigid follicle movements from TPLSM image stacks with the vibrissa in reference and deflected positions, and then performing particle image velocimetry between the pairs of aligned and transformed image stacks. All data and statistical analysis was performed with MATLAB (MathWorks), and utilized computational resources at the San Diego Supercomputer Center.

Unless otherwise stated, averages refer to arithmetic means and tests for significance were performed using two-sample T-tests. Comparisons between displacement fields as a function of follicle location and deflection direction, and interactions thereof, were evaluated by one- or two-way repeated measures ANOVA.

# Results

## Tissue labeling and mechanoreceptor distribution

Individual follicles are innervated by two sets of nerve (**Fig. 1**). With reference to visualization of the follicle from an *Advillin*$^{Cre/+}$ mouse line crossed with a RFP reporter (**Fig. 1a,b),** and in agreement with prior studies (Ebara et al., 2002; Rice et al., 1986; Sakurai et al., 2013), a single, large deep vibrissa nerve (DVN) innervates Merkel cells that are located in the outer root sheath (ORS). The nerve attaches to these cells at the level of the ring sinus (RS) between the ringwulst (RW) and the inner conical bodies (ICBs). The Merkel dense region (MDR) and the ringwulst below it are the focus of this study. The afferent attachments to the Merkel cells as well as longitudinal lanceolate endings are preferentially labeled in Thy1-TN-XXL mice (**Fig. 1c**). The deep vibrissa nerve further innervates the mesenchymal sheath (MS), to which the ringwulst is attached, with club-like endings and innervates the cavernous sinus (CS) as free-nerve endings (Ebara et al., 2002; Sakurai et al., 2013). In contrast to the deep nerve, small superficial vibrissa nerves innervate Merkel cells at the rete ridge collar (RRC) and the inner and outer conical bodies (OCBs) and attach as both lanceolate and free-nerve endings.

The structure of the Merkel dense region was investigated in a whole-mount with part of the outer connective tissue sheath of the follicle micro-dissected (**Fig. 1d**) and all nuclei stained with DAPI (**Fig. 1e**). Longitudinal and radial cross sections revealed four distinct layers of labeled tissue (**Fig. 1f,g**). An outer ring, 10 to 20 µm thick and contiguous with the ringwulst, was identified as the mesenchymal sheath. An unlabeled 10 µm thick ring, identified as the glassy membrane, separated the mesenchymal from the outer root sheath. We identified two DAPI labeled cylindrical shells within the outer root sheath with different thicknesses and nuclear densities. The external cylinder, which we will refer to as $ORS_e$, was 10 to 15 µm and contained the elongated cell nuclei of putative Merkel cells. The internal cylinder, referred to as $ORS_i$, was ~ 10 µm thick and was sparsely populated by cell nuclei of an unknown type. The internal root sheath (IRS), which surrounds the vibrissa shaft, was unlabeled. Thus, we conclude that DAPI labeling was restricted to cylindrical layers that are known to be innervated by deep vibrissa nerve afferents (Ebara et al., 2002; Rice et al., 1986). The restricted and bright labeling of nuclei within the Merkel dense region by DAPI, as opposed to genetic labeling of the cytoplasm throughout the Merkel cells (***cf* panels b and e in Fig. 1**), suggests that the former labeling is a better choice for our analysis of displacement fields.

**Internal vibrissa shaft deformations**

The vibrissa-follicle junction is reported to be rigid during whisking against an object (Bagdasarian et al., 2013) and the vibrissa shaft is reported to flex within the follicle during passive vibrissa deflection (Ebara et al., 2002; Wrobel, 1965). We confirmed both of these observations in follicles fixed with preservative *in vivo* while all vibrissae were deflected in either the rostral or caudal directions (**Fig. 1h,i**). We observe that the superficial internal segment of the vibrissa shaft, which extends from the rete ridge collar down to the ringwulst, is indeed rigid, and that the deep segment, which extends below the level of the ring sinus, bends during rostral but not caudal deflections. These observations are consistent with the report by Ebara et al. (Ebara et al., 2002) that "*the follicle is soft at the lower level of the cavernous sinus and gradually becomes more rigid toward and through the level of the ring sinus*". In the present study it is of relevance that the shaft of the vibrissa remains straight across the Merkel dense region

(**Fig. 1i**).

**Relative displacements during static vibrissa deflection**

Freshly dissected follicles, with a window cut through the outer capsule wall, were stained with DAPI and pinned so that TPLSM image stacks of DAPI fluorescence could be acquired during rest and with 10° and 20° deflections of the vibrissa in both the caudal and rostral directions (**Fig. 1d**). We alternated the acquisition of data between the rest position and a given deflection (**Fig. 2a**). We assumed that the total transformation describing the motion of the follicle in response to a deflection of the vibrissa is the sum of a rigid body transformation and localized deformations.

Automated cell tracking was used to locate the centroids of labeled nuclei (**Fig. 2b**). Approximately 150 corresponding nuclei per image stack, evenly distributed throughout the field of view, were manually matched across reference and deflection image stacks for each cell. The nuclei in the deflected stack, with position vectors $\mathbf{x}'$, were optimally aligned to the corresponding nuclei in the reference stack, with position vectors $\mathbf{x}$, by adjusting three translational and three rotational degrees of freedom in a rigid transformation (**Fig. 2c**). Formally, $\mathbf{x}' = \Delta\mathbf{x} + \mathbf{R}(\theta,\varphi,\zeta)\,\mathbf{x}$, where $\Delta\mathbf{x}$ is the translation vector and $\mathbf{R}$ is the rotation matrix that is parameterized by the Tait-Bryan angles θ, φ, and ζ with

$$\mathbf{R} = \begin{bmatrix} \cos(\theta) & -\sin(\theta) & 0 \\ \sin(\theta) & \cos(\theta) & 0 \\ 0 & 0 & 1 \end{bmatrix} \begin{bmatrix} 1 & 0 & 0 \\ 0 & \cos(\varphi) & -\sin(\varphi) \\ 0 & \sin(\varphi) & \cos(\varphi) \end{bmatrix} \begin{bmatrix} \cos(\zeta) & 0 & -\sin(\zeta) \\ 0 & 1 & 0 \\ -\sin(\zeta) & 0 & \cos(\zeta) \end{bmatrix}$$

. Larger deflections consistently result in larger rigid transformations and, as a control, re-alignment of paired stacks of reference images produced qualitatively high overlap between the corresponding cells.

The difference between the reference stack and the optimally realigned deflection stack defines the local displacement of the tissue caused by deflection of the vibrissa. We determined the displacement vectors with particle image velocimetry calculated with the use of 25×25×25 $\mu m^3$ voxels that typically contained three or more reference cell nuclei. The spatial lags of the cross-correlation between the reference and aligned deflected data sets were computed continuously for each image pixel at location $(x,y,z)$. Each cross-correlation typically contained a single, local peak whose offset from the

origin corresponded to the displacement vector field $\mathbf{u}(x,y,z)$ (**inset Fig. 2c**). The displacement vectors are the essential result of the analysis. For the data of **Figure 2b,c**, the root-mean-square length of the displacement vectors was 4.4 ± 2.5 μm (mean ± SD) (**Fig. 2d**).

The displacement vectors were conditioned prior to further analysis. First, vectors with magnitudes greater than three standard deviations above the mean, *i.e.*, ~ 12 μm for the data of **Figure 2b-d**, were considered outliers and removed. Second, the field formed by the displacement vectors was slightly smoothed with a Gaussian filter with $\sigma$ = 15 μm; voxels without a cell nucleus or otherwise incomplete data were not interpolated. Lastly, we fitted a cylindrical annulus that was aligned to the principal axis of the vibrissa shaft (**Fig. 2e**) to extract only the relevant tissue that, further, may be mapped onto a plane for improved visualization. A 95 ± 5 μm thick region, that exclusively encompassed the outer root sheath, the mesenchymal sheath, and the glassy membrane parts of the ringwulst, was extracted for further analysis (**Fig. 1f)**. The displacement fields were transformed from their Cartesian coordinates into cylindrical coordinates as radial projections (**Fig. 2e**). The radial distance, $r$, is the perpendicular distance from the principal axis and the radial displacement, $\Delta r$, is the change in $r$ after deflection of the vibrissa (**Fig. 2f,g**). The polar angle, $\alpha$, is the offset from the vertical axis such that $-\pi/2$ and $\pi/2$ indicate the caudal and rostral aspects of the follicle, respectively, and the polar displacement, $\Delta\alpha$, is the change in angular offset after deflection. The longitudinal coordinate, $l$, is the location along the axis and the longitudinal displacement, $\Delta l$, is the change in this coordinate after deflection.

Example displacement fields computed from images of the follicle at rest and during a 10° caudal deflection are shown in **Figure 2g**. The upper and lower halves of the displacement fields correspond approximately to the Merkel cell dense and ringwulst regions, respectively (**Fig. 2f**). Three main characteristics were observed. First, tissue was radially displaced outwards and inwards along the caudal and dorsal aspects of the follicle, respectively, suggesting a relative flattening of the follicle (**left, Fig. 2g**). Second, the tissue underwent a relative counter rotation in the Merkel dense and ringwulst regions of the mesenchymal and outer root sheaths (**middle, Fig. 2g**). Lastly, the ringwulst and Merkel dense regions differed in the direction of longitudinal

displacement, such that the deeper ringwulst tissue was displaced laterally outward towards the skin while the more superficial Merkel dense region was shifted medially inward away from the skin (**right, Fig. 2g**). Individual trials within a single experiment were highly repeatable, as shown by the standard error compared to displacement magnitudes (**insets Fig. 2g).**

Displacement maps for each condition of deflection and amplitude were aligned and averaged across experiments. Image stacks acquired with right-side follicles were mirrored prior to averaging. As there are no sharp boundaries to delineate regions along the principal axis of the follicle, seven naive observers manually aligned the data sets by matching pairs of DAPI fluorescence images. Alignments were in agreement across observers, and the optimal offset $d_i$ for each image to a reference image was found by minimizing the sum of squares across $U$ users and $N$ images, *i.e.*, $\min \sum_{\substack{1 \le i \le j \le N \\ U}} (\mathbf{O}_{ijU} - (d_j - d_i))^2$, where $\mathbf{O}_{ijU}$ is the alignment for one pair of images from one observer.

*Radial tissue displacements*

The tissue displaced outwards along the caudal edge of the follicle during caudal deflections and outwards towards the rostral edge during rostral deflections. Thus, radial displacements in the ring sinus region follow the direction of vibrissa deflection at a ratio of ~ 0.3 μm per degree (**left column Fig. 3**); these effects are significant at the location of the ringwulst, *i.e.*, $F(1,36) = 8.3$ ($p = 0.007$), and the Merkel dense region, *i.e.*, $F(1,36) = 34.5$ ($p < 0.001$). Additionally, we observed inward radial displacements on the order of 0.1 μm per degree along the dorsal edge of the follicle that were invariant of deflection direction.

*Polar tissue displacements*

Polar displacements in the Merkel dense region had opposite sign in the dorsocaudal and dorsorostral quadrants, with $F(1,36) = 15.0$ ($p < 0.001$), independent of the direction of vibrissa deflection. Displacements in the ringwulst region, however, were statistically different during caudal and rostral deflections, with $F(1,36) = 17.0$ ($p < 0.001$), but not as a function of location. Thus, mesenchymal and outer root sheath tissue rotate about the

axis of the vibrissa in the direction of vibrissa deflection at a ratio of ~ 0.17° per degree of vibrissa deflection, where the direction of rotation in the ringwulst is dependent on deflection direction (**middle column, Fig. 3**).

*Longitudinal tissue displacements*

Longitudinal displacements in the Merkel dense region were invariably in the medial direction, *i.e.*, inwards, regardless of vibrissa deflection direction and amplitude. In the ringwulst region, the direction of longitudinal displacement differed between directions of the deflection, with $F(1,36) = 5.74$ ($p = 0.022$), but the displacement was not significantly different between the dorsocaudal and dorsorostral quadrants. Thus, the Merkel dense region undergoes inward longitudinal displacement during vibrissa deflection that is invariant of direction, while the ringwulst region undergoes directional selective longitudinal displacements. These displacements are on the order of ~ 0.3 μm per degree (**right column Fig. 3**).

**Strains during vibrissa deflection**

The displacements in the follicle that we observed were coherent over length scales much larger than that of single cells (**Fig. 3**). Thus, sites of mechanotransduction during vibrissa deflection cannot be inferred from displacement measurements alone. As a means of estimating local volumetric deformations, we calculated the volumetric strain field, which is a scalar quantity measuring uniform dilation or compression at a point in space, from the measured displacements. The volumetric strain field is found by computing the spatial derivatives of the displacement vector field that contribute to the fractional change in volume (Landau and Lifshitz, 1959), *i.e.*, $\Delta V/V = \partial \mathbf{u}_1(x,y,z)/\partial x_1 + \partial \mathbf{u}_2(x,y,z)/\partial x_2 + \partial \mathbf{u}_3(x,y,z)/\partial x_3$, where the index labels the direction of the vector at each point $(x,y,z)$.

As a means to minimize inelastic deformations of the follicle from repeated vibrissa deflections, we computed strain fields from control trials in which displacements were calculated across two image stacks with the vibrissa in the rest position taken before and after a vibrissa deflection. This control strain field was then subtracted from each strain field computed from displacement maps that compared a follicle in its rest and deflected positions. We then averaged computed strain fields across all follicles,

grouped by vibrissa deflection direction and amplitude as in the case of the underling displacement fields (**Fig. 3**). Standard errors were typically on the order of the variations across the strain field for a single follicle, and were generally larger along the caudal and rostral edges of the follicle since fewer features were available for the strain computation. We focus on the data sets with a 10° deflection of the vibrissa as these consistently showed less variability (**insets, Fig. 3**).

Strain in the ringwulst region was predominantly negative, indicating compression, and ranged between 0.005 to 0.03 on average in magnitude for a 10° deflection. In contrast, strain in the Merkel denser region varied from negative to positive (**Fig. 4a,b**). We averaged and compared strain across the four quadrants of the dorsal half of the follicle, which approximately correspond to the rostral ($R^{RW}$) and caudal ringwulst ($C^{RW}$), and the rostral ($R^{MDR}$) and caudal ($C^{MDR}$) Merkel dense region (**Fig. 4a**). We found no statistically significant difference in strain between quadrants within or across deflection conditions. We found, however, a statistically significant interaction among mean strains from diagonal quadrants, with $F(1,20) = 6.2$ ($p = 0.022$), which implies correlations in the variability across quadrants. This interaction is interpreted as a preferential gradient of strain with a magnitude of ~ 0.02 ΔV/V across the ring sinus region that shifts in orientation between deflection direction (**Fig. 4c**). During caudal deflections, tissue compressed in the rostral ringwulst region ($R^{RW}$) and dilated in the caudal MDR ($C^{MDR}$) (**left Fig. 4b**). During rostral deflections, tissue compressed in the caudal ringwulst region ($C^{RW}$) and dilated in the rostral MDR ($R^{MDR}$) (**right Fig. 4b**). Similar results were observed for a 20° deflection. This leads to the crux result, *i.e.*, the direction of vibrissa deflection is encoded mechanically in the follicle by a longitudinally diagonal rostrocaudal gradient of strain.

## Discussion

We analyzed tissue displacements in cylindrical coordinates and found that the tissue is displaced differentially in the radial, polar and longitudinal directions during vibrissa deflections (**Fig. 2e**). Specifically, we find that cells rotate about the axis of the vibrissa shaft and are displaced radially in the direction of deflection (**Fig. 3**). Furthermore, longitudinal displacements within the ringwulst region reverse between

caudal and rostral vibrissa deflections. Additionally, we observed significant direction invariant displacements (**Fig. 3**). As mechanoreceptors may not respond to tissue displacements, we computed volumetric strain as a measure of tissue deformation and thus an indirect predictor of mechanoreceptor activation. We find that vibrissa deflection leads to a gradient of strain across the Merkel dense and ringwulst regions, and that the orientation of this gradient rotates when deflection direction changes (**Fig. 4**). Rice and Munger (Rice and Munger, 1986) hypothesized that as a deflected vibrissa pivots about a fulcrum close to the skin, and moves in the opposite direction in the ring sinus, the mesenchymal sheath and attached lanceolate endings are compressed on the leading edge and stretched elsewhere. Our observations are consistent with this prediction, as we find that during a caudal deflection the tissue compresses in the rostral (leading) segment of the ringwulst and dilates in the caudal region close to the inner conical body. During a rostral deflection, this diagonal gradient is mirrored.

The differential strain that we observe should exert different displacement patterns within the domain of the Merkel endings that originate from the axonal terminal field of a single neuron. It is of interest that a given Aβ fiber terminates on multiple, neighboring Merkel cells that span only a fraction of the follicle, with different fibers labeling different parts of the follicle. In contrast, Aβ fiber innervation exhibits a much broader pattern in the vibrissae of the cat, which does not whisk (Ebara et al., 2002). In general, the amalgam of past anatomical data and the present results suggests that each of the myriad of directions and amplitudes of motion of the vibrissa that occur when a rodent sweeps it's vibrissae across objects is encoded as a particular pattern of afferent input.

**Methodological considerations**

We labeled cells in the follicle-sinus complex with the fluorescent nuclear stain DAPI. Nerves were therefore not labeled and labeling did not distinguish between different mechanoreceptor types. While this precludes direct measurements of mechanoreceptor deformation, we find that displacement and strain fields were coherent on spatial scales larger than individual cells (**Figs. 3 and 4**). Applied mechanical pressure can be sensed by Merkel cells through layers of intervening cells

419 (Ikeda and Gu, 2014). Thus, we assume that tissue deformations observed on the
420 spatial scale of tens of microns reflect the stresses experienced by individual
421 mechanoreceptors.

422 Head and body movements may substitute for vibrissa movements when
423 scanning surfaces (Krupa et al., 2001). Further, rats can make amplitude and velocity
424 discriminations during passive vibrissa stimulation (Fassihi et al., 2014; Stüttgen et al.,
425 2006). Thus, vibrissa deflection without an active muscular contribution is a feature of
426 normal sensory experience. During whisking, the vibrissae are actively moved and
427 pushed against surfaces by the contractile actions of facial muscles (Hill et al., 2008).
428 Tissue mechanics and internal deformations of the follicle may therefore be very
429 different during active touch as compared to passive vibrissa deflection, as employed
430 here.

431 **Relationship between strain measurements and mechanosensitivity**

432 Mechanosensitivity of the Merkel-neurite complex and lancelolate endings in hairy skin
433 is mediated by the Piezo2 mechanosensitive cation channel (Coste et al., 2010; Lou et
434 al., 2013). Merkel cells in the rat follicle-sinus complex have recently been shown to
435 actively transduce movements of the vibrissae via Piezo2, assumed to be located on
436 Merkel cell processes, and drive Aβ afferents via $Ca^{2+}$-based action potentials and the
437 presumptive release of an, as of yet, unidentified neurotransmitter (Ikeda et al., 2014;
438 Ikeda and Gu, 2014; Maksimovic et al., 2014). Mechanically activated currents have
439 been measured in Piezo2 expressing cultured dorsal root ganglion neurons (Coste et
440 al., 2010) during cell membrane displacements down to 10 nm (Poole et al., 2014). As
441 an order-of magnitude estimate of the associated volumetric strain, we take the radial
442 cross-section of ganglion neuron processes to be 2 μm, for which a 10 nm membrane
443 deflection yields $\Delta V/V \approx \Delta L/L \approx 5x10^{-4}$. We observe strain with magnitudes in the range
444 of 0.02 to 0.05 during 10° angular vibrissa deflections (**Fig. 4b,c**). The minimum
445 deflection for an electrophsyiological response in trigeminal fibers is stated to be 0.1°
446 (Gibson and Welker, 1983), which by linear extrapolation is a strain with magnitude in
447 the range of $2x10^{-4}$ to $5x10^{-4}$. Thus the sensitivity for vibrissa touch in mouse is
448 consistent with the threshold to activate Piezo2 mediated membrane currents in Merkel
449 cell afferents.

## Acknowledgements

We thank Yoav Freund and Congjun Wu for advise on analysis and computing, Fan Wang for the *Advillin*$^{Cre/+}$ mice, Oliver Griesbeck for the Thy1-TN-XXL mice, and an anonymous reviewer for thoughtful comments and discussion points. Our work was funded by the United States National Institutes of Health (grants NS058668 and NS066664), the United States National Science Foundation (grant PHY-1451026), the United States and Israeli Binational Science Foundation (grant 2003222), and the Extreme Science and Engineering Discovery Environment for use of the San Diego Supercomputing Center Gordon Computing Cluster (grant IBN140016).

## Conflicts of Interest

None

## Contributions

All authors planned the experiments. The data was obtained by DWM and SJW, analyzed by SJW, and the manuscript was written by DK, PMK and SJW. In addition, DK dealt with the myriad of university rules and forms that govern environmental health and safety, hazard control, and the use of animals, chemicals, controlled substances, hazardous substances, and lasers, as well as protocols through the institutional animal care and use committee and directives on ethical conduct in the workplace.

## References


**Abraira VE, Ginty DDT**. The sensory neurons of touch. Neuron 79:618–639. 2013.

**Bagdasarian K, Szwed M, Knutsen PM, Deutsch D, Derdikman D, Pietr M, Simony E, Ahissar E**. Pre-neuronal morphological processing of object location by individual whiskers. Nature Neuroscience 16:622-631. 2013.

**Coste B, Mathur J, Schmidt M, Earley T**. Piezo1 and Piezo2 are essential components of distinct mechanically activated cation channels. Science 330:55-60. 2010.

**da Silva S, Hasegawa H, Scott A, Zhou X, Wagner AK, Han BX, Wang F**. Proper formation of whisker barrelettes requires periphery-derived Smad4-dependent TGF-beta signaling. Proceedings of the National Academy of Sciences USA 22:3395-3400. 2011.

**Ebara S, Kumamoto K, Matsuura T, Mazurkiewicz JE, Rice FL**. Similarities and differences in the innervation of mystacial vibrissal follicle-sinus complexes in the rat and cat: A confocal microscopic study. Journal of Comparative Neurology 449:103-119. 2002.

**Fassihi A, Akrami A, Esmaeili V, Diamond ME**. Tactile perception and working memory in rats and humans. Proceedings of the National Academy of Sciences USA 111:2331–2336. 2014.

**Gibson JM, Welker WI**. Quantitative studies of stimulus coding in first-order vibrissa afferents of rats. 1. Receptive field properties and threshold distributions. Somatosensory Research 1:51-67. 1983.

**Hill DN, Bermejo R, Zeigler HP, Kleinfeld D**. Biomechanics of the vibrissa motor plant in rat: Rhythmic whisking consists of triphasic neuromuscular activity. Journal of Neuroscience 28:3438-3455. 2008.

**Hires SA, Pammer L, Svoboda K, Golomb D**. Tapered whiskers are required for active tactile sensation. Elife 2:e01350. 2013.

**Ikeda R, Cha M, Ling J, Jia Z, Coyle D, Gu JG**. Merkel cells transduce and encode tactile stimuli to drive Aβ-afferent impulses. Cell 157:664–675. 2014.

**Ikeda R, Gu JG**. Piezo2 channel conductance and localization domains in Merkel cells of rat whisker hair follicles. Neuroscience Letters 583:210–215. 2014.

**Johnson KO**. The roles and functions of cutaneous mechanoreceptors. Current Opinions n Neuroscience 11:455–461. 2001.

**Jones LM, Depireux DA, Simons DJ, Keller A**. Robust temporal coding in the trigeminal system. Science 204:1986-1989. 2004.

**Kleinfeld D, Delaney KR**. Distributed representation of vibrissa movement in the upper layers of somatosensory cortex revealed with voltage sensitive dyes. Journal of Comparative Neurology 375:89-108. 1996.

**Krupa DJ, Matell MS, Brisben AJ, Oliveira LM, Nicolelis MAL**. Behavioral properties of the trigeminal somatosensory system in rats performing whisker-dependent tactile discriminations. Journal of Neuroscience 21:5752-5763. 2001.

Landau LD, Lifshitz EM. 1959. Theory of Elasticity. New York: Plenum Press.

**Li L, Rutlin M, Abraira VE, Cassidy C, Kus L, Gong S, Jankowski MP, Luo W, Heintz N, Koerber HR, Woodbury CJ, Ginty DD**. The functional organization of cutaneous low-threshold mechanosensory neurons. Cell 147:1615-1627. 2011.

**Lichtenstein SH, Carvell GE, Simons DJ**. Responses of rat trigeminal ganglion neurons to movements of vibrissae in different directions. Somatosensory and Motor Research 7:47-65. 1990.

**Lou S, Duan B, Vong L, Lowell BB, Ma Q**. Runx1 controls terminal morphology and

mechanosensitivity of VGLUT3-expressing C-mechanoreceptors. Journal of Neuroscience 33:870-882. 2013.

**Madisen L, Zwingman TA, Sunkin SM, Oh SW, A. ZH, Gu H, Ng LL, Palmiter RD, Hawrylycz MJ, Jones AR, Lein ES**. A robust and high-throughput Cre reporting and characterization system for the whole mouse brain. Nature Neuroscience 13:133-140. 2010.

**Maksimovic S, Nakatani M, Baba Y, Nelson AM, Marshall KL, Wellnitz S, Firozi P, Woo S-H, Ranade S, Patapoutian A, E. L**. Epidermal Merkel cells are mechanosensory cells that tune mammalian touch receptors. Nature 509:617–621. 2014.

**Mank M, F. SA, Direnberger S, Mrsic-Flogel TD, Hofer SB, Stein V, Hendel T, Reiff DF, Levelt C, Borst A, Bonhoeffer T, Hübener M, Griesbeck O**. A genetically encoded calcium indicator for chronic *in vivo* two-photon imaging. Nature Methods 5:805-811. 2008.

**Mitchinson B, Arabzadeh E, Diamond ME, Prescott TJS**. pike-timing in primary sensory neurons: a model of somatosensory transduction in the rat. Biological Cybernetics 98:185-194. 2008.

**Mitchinson B, Gurney KN, Redgrave P, Melhuish C, Pipe AG, Pearson M, Gilhespy I, Prescott TJ**. Empirically inspired simulated electro-mechanical model of the rat mystacial follicle-sinus complex. Proceedings of the Royal Society: Bioilogical Sciences 271:2509-2516. 2004.

**O'Connor DH, Clack NG, Huber D, Komiyama T, Myers EW, Svoboda K**. Vibrissa-based object localization in head-fixed mice. Journal of Neuroscience 30:1947-1967. 2010.

**Poole K, Herget R, Lapatsina L, Ngo H-D, Lewin GR**. Tuning Piezo ion channels to detect molecular-scale movements relevant for fine touch. Nature Communications 5:3520. 2014.

**Quist BW, Hartmann MJZ**. Mechanical signals at the base of a rat vibrissa: The effect of intrinsic vibrissa curvature and implications for tactile exploration. Journal of Neurophysiology 107:2298–2312. 2012.

**Rice FL, Mance A, Munger BL**. A comparative light microscopic analysis of the sensory innervation of the mystacial pad. I. Innervation of vibrissal follicle-sinus complexes. Journal of Comparative Neurology 252:154-174. 1986.

**Rice FL, Munger BL**. A comparative light microscopic analysis of the sensory innervation of the mystacial pad. II. The common fur between the vibrissae. Journal of Comparative Neurology 252:186–205. 1986.

**Sakurai K, Akiyama M, Cai B, Scott A, Han B-X, Takatoh J, Sigrist M, Arber S, Wang F**. The organization of submodality-specific touch afferent inputs in the vibrissa column. Cell Reports 5:87-98. 2013.

**Shoykhet M, Doherty D, Simons DJ**. Coding of deflection velocity and amplitude by whisker primary afferent neurons: Implications for higher level processing. Somatosensory and Motor Research 17:171-180. 2000.

**Stüttgen MC, Rüter J, Schwarz C**. Two psychophysical channels of whisker deflection in rats align with two neuronal classes of primary afferents. Journal of Neuroscience 26:7933-7941. 2006.

**Szwed M, Bagdasarian K, Ahissar E**. Coding of vibrissal active touch. Neuron 40:621-630. 2003.

**Woodbury C, Koerber H**. Central and peripheral anatomy of slowly adapting type I low□threshold mechanoreceptors innervating trunk skin of neonatal mice. Journal of Comparative Neurology 561:547–561. 2007.

**Wrobel K**. Bau und Bedeutung der Blutsinus in den Vibrissen von Tupaia glis. Zentralblatt für Veterinärmedizin 12:888-899. 1965.

## Figure legends

**Figure 1. Mouse follicle-sinus complex anatomy and mechanoreceptor distribution. a.** Anatomical features of the mouse follicle. Merkel cells were selectively labeled with RFP in *Advillin*$^{Cre/+}$ knockin mice, and 100 µm thick serial sections imaged on a light microscope. Annotations: Rete ridge collar, RRC; outer conical body, OCB; inner conical body, ICB; Merkel cell dense region, MDR; mesenchymal sheath, MS; ring sinus, RS; ringwulst, RW; deep vibrissal nerve, DVN; intrinsic muscle, IM; cavernous sinus, CS; vibrissa shaft, VS; hair bulb, HB; hair papilla, HP. Scale bar is 500 µm. **b.** Maximum projection of a confocal image stack through the MDR of an *Advillin*$^{Cre/+}$ knockin mouse crossed with an RFP reporter mouse. The Merkel cells are located at the level of the RS between the ringwulst and the ICB. Scale bar is 100 µm. Inset shows a magnified view of a single confocal layer close to the edge of the ring sinus, demonstrating that Merkel cells are located in the outer root sheath (ORS). Glassy membrane (unlabeled) is located between the ORS and the mesenchymal sheath (MS). Scale bar is 10 µm. **c.** Maximum projection of a confocal image stack of the RS region in a Thy1-TN-XXL transgenic mouse with labeled Merkel and lanceolate ending afferents. Scale bar is 100 µm. **d.** Schematic of a micro-dissected follicle row pinned to a silicon base immersed in aCSF for two-photon imaging. The imaged follicle was suspended above a gap in the silicone base to minimize friction during vibrissa deflection (arrow). **e.** Maximum projection of a TPLSM acquired image stack of a DAPI labeled vibrissa follicle. A window was opened in the vibrissa capsule above the dorsal aspect of the RS to expose the region between the RW and the ICB. Scale bar is 100 µm. Inset shows a zoomed in region containing horizontally elongated cell nuclei that were classified as putative Merkel cells. Scale bar is 10 µm. **f.** Longitudinal cross-section through the image stack in panel e. Layers of tissue were identified based on DAPI labeling: the mesenchymal sheath (MS), glassy membrane (GM) and outer root sheath (ORS). The inner root sheath (IRS) was never labeled by DAPI. Scale bar is 100 µm. **g.** Radial cross-section through the image stack in panel e, demonstrating the same DAPI labeled layers as in panel f. Scale bar is 20 µm. **h.** Fixed and sectioned FSC tissue labeled with the membrane dye 5-hexadecanoylamino-fluorescein (H-110). The mouse was perfused and fixed while the vibrissa was deflected in either the caudal (top) or rostral (bottom) directions. Note how the vibrissa shaft buckles and bends in the region of the cavernous sinus only during rostral deflections. Black arrows indicate the intrinsic sling muscle. Scale bars are 500 µm.

**Figure 2. Measuring relative displacements and strain within the follicle-sinus complex.**

**a.** Cartoon of the vibrissa in a follicle-sinus complex. The Merkel cell dense region under study is in red and green. **b, top.** Maximum projection of the raw image stacks acquired with the vibrissa in its reference, rest, position (red) and when deflected 10° in the caudal direction (green). R, M, and V indicate the rostral, medial, and ventral directions, respectively. Inset is a magnified image of the enclosed region in white, demonstrating rigid rotation and translation of individual DAPI labeled cell nuclei (yellow denotes overlap). **b, bottom.** Maximum projections of radial sections along the longitudinal direction of the follicle. **c, top.** Maximum projection of the same image stacks after rigid alignment of the deflected stack onto the reference stack through a rigid transformation with six degrees of freedom. Inset is a magnified region (same as in panel a) demonstrating remaining relative movements that cannot be corrected by the transformation (red or green pixels). **c, bottom.** Maximum projections of radial sections along the longitudinal direction of the follicle. **d.** Distribution of displacement vector magnitudes of individual pixels from a single vibrissa deflection, computed from 3D cross-correlations between aligned image stacks (see *Methods*). **e.** The coordinate system of pixel displacement vectors. Each pixel was displaced in three directions, in a vibrissa-oriented coordinate system: radial ($\Delta r$) perpendicular to the vibrissa shaft (red cylinder), polar ($\Delta\alpha$) about the axis of the vibrissa (red circle), and longitudinal ($\Delta l$) along the axis of the vibrissa. DAPI labeled cells included in the analysis were all located within a 90 – 100 μm thick annulus approximately bounded by the MS and ORS (green cylinder with single planar imposed imposed on front surface; gray cells are outside the included volume). **f.** Aligned and transformed image of DAPI labeled pixels included in analysis of displacement and strain fields in a single experiment. The approximate extents of the Merkel cell dense region (MDR) and ringwulst (RW) are indicated. Gray pixels indicate pixels in which none or insufficient data was available to compute displacements. **g.** Displacement analysis of 10° vibrissa deflection in the caudal direction in a single experiment. Displacements of individual pixels were transformed from Cartesian coordinates into cylindrical coordinates, and then displacements in the radial, polar, and longitudinal directions were averaged across pixels in the radial direction. Note that all displacement maps extend from approximately $-\pi/2$ to $\pi/2$, which corresponds to the caudal and rostral aspects of the follicle respectively. *Left.* Radial displacements, $\Delta r$, with positive (red/yellow) and negative (blue/white) corresponding to outward and inwards displacements, respectively. *Middle.* Polar displacements, $\Delta\alpha$, with positive and negative values indicating anterior and posterior rotation over the dorsal side of the vibrissa shaft, respectively. *Right.* Longitudinal displacements, $\Delta l$, with positive and negative values indicating inward and outward motion along the axis of the vibrissa, respectively. Displacement field averages were smoothed with a square boxcar mean filter (20 μm width/height). Insets

634 show the standard error computed across repetitions of the same deflection (n = 3 trials).
635
636 **Figure 3. Population analysis of displacement fields.** Radial, polar, and longitudinal
637 displacement fields were averaged across follicles by vibrissa deflection direction, *i.e.*, caudal or
638 rostral, and amplitude, *i.e.*, 10° or 20°. The number of deflection conditions varied between
639 experiments. Thus, the number of follicles included in each panel was as follows: caudal 10°
640 (n = 7); caudal 20° (n = 4); rostral 10° (n = 5); and rostral 20° (n = 4). Displacement field
641 averages were smoothed by a square mean filter (20 μm width/height). Vertical dashed lines
642 indicate the axis of the vibrissae. Scale bar is 100 μm.
643
644 **Figure 4. Population analysis of strain fields. a.** Raw DAPI fluorescence image aligned and
645 averaged across follicles and then transformed into cylindrical coordinates (see *Methods*). The
646 boundary between the ringwulst (RW) and Merkel cell dense region (MDR) is indicated by the
647 curved, solid white line. Vertical dashed line indicates the center axis of the vibrissa shaft (VS).
648 Scale bar is 100 μm. **b.** Strain fields were averaged across follicles, by vibrissa deflection
649 direction (caudal or rostral). The number of follicles included in each panel is as in **Figure 3**.
650 Strain field averages were smoothed by a square median filter across 100 μm. The cartoons
651 indicate the direction of deflection and the area (green) for which volume strains were
652 computed. **c.** Gradients of mean strain across diagonal quadrants in the follicle. Dashed lines
653 are individual follicles and solid lines are averages.
654

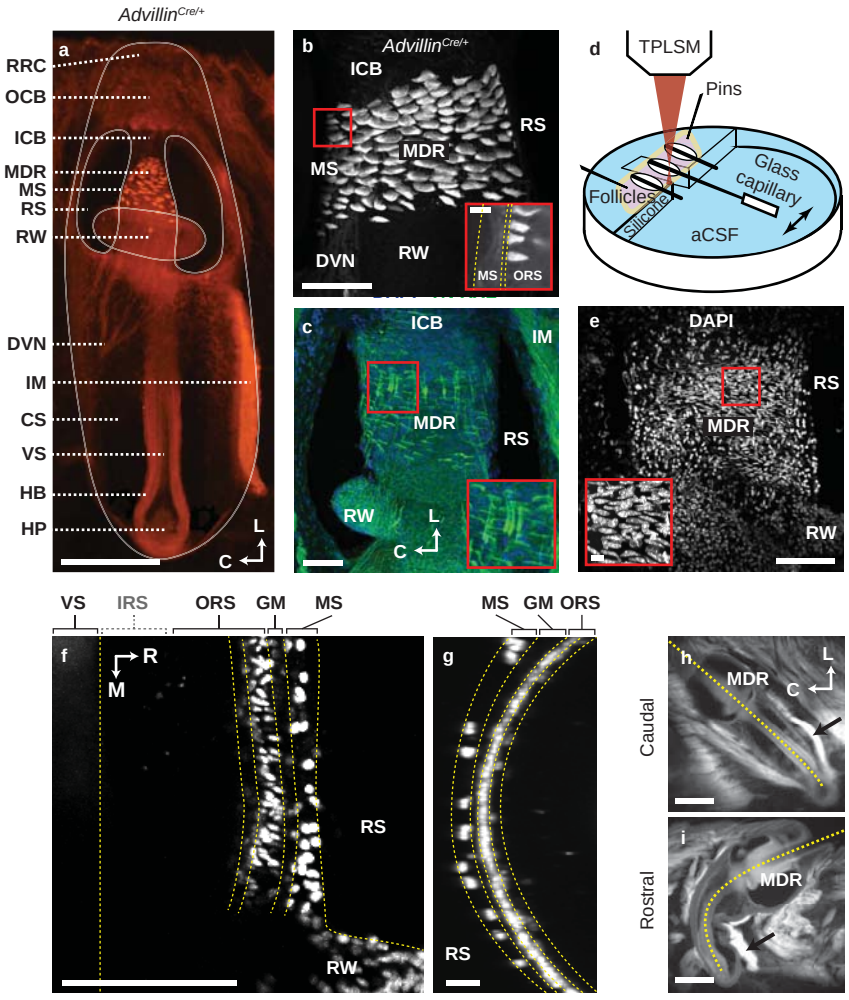


Figure 1. Whiteley, Knutsen, Matthews & Kleinfeld

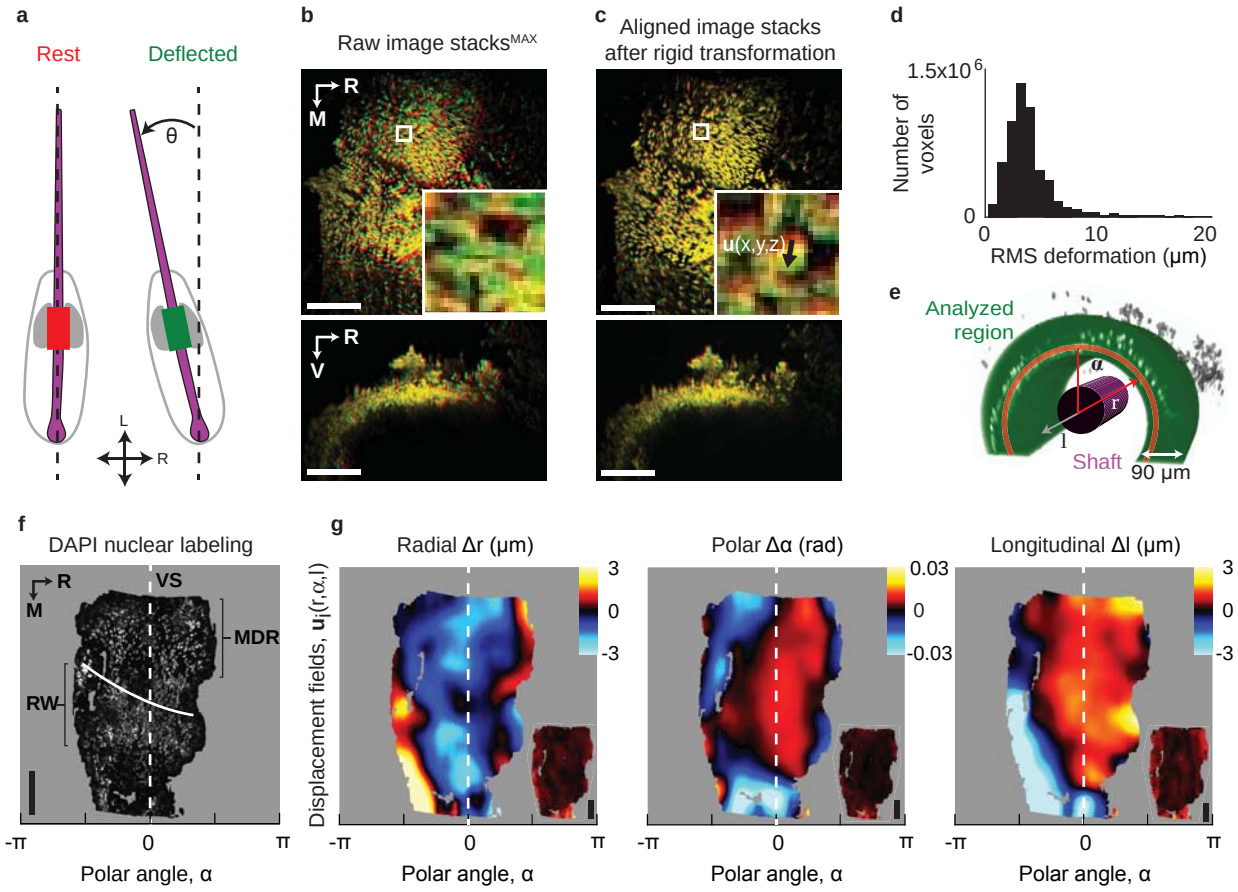


Figure 2r. Whiteley, Knutsen, Matthews & Kleinfeld

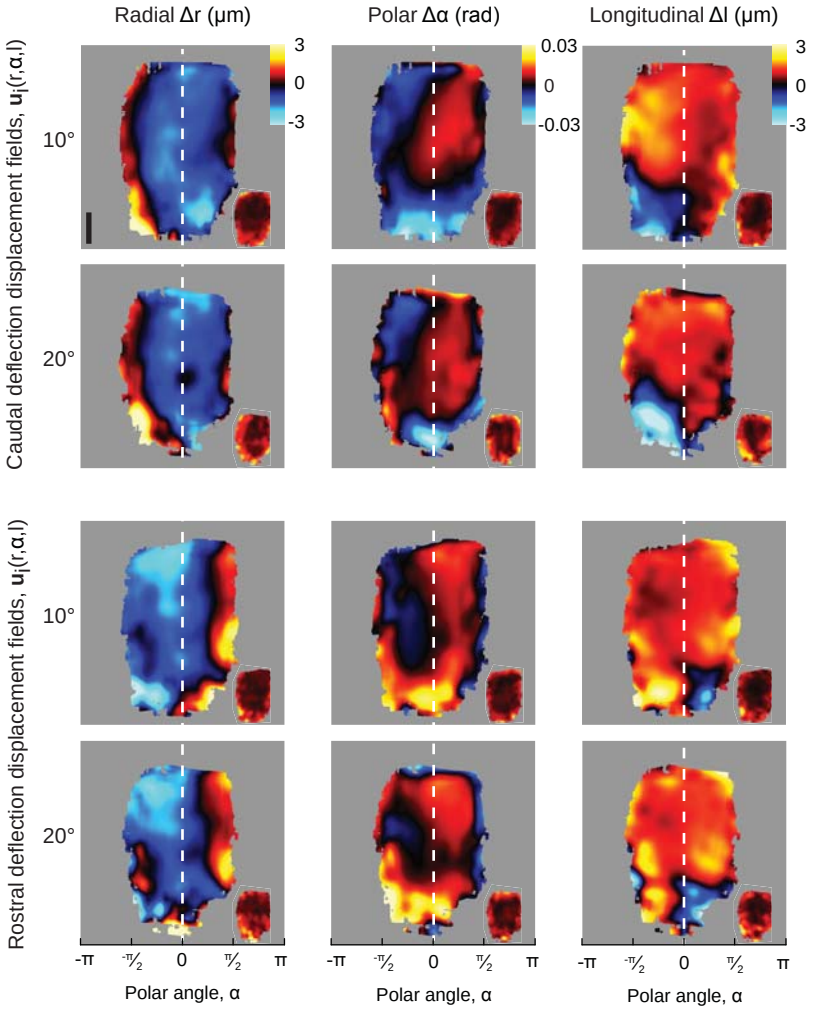


Figure 3. Whiteley, Knutsen, Matthews & Kleinfeld

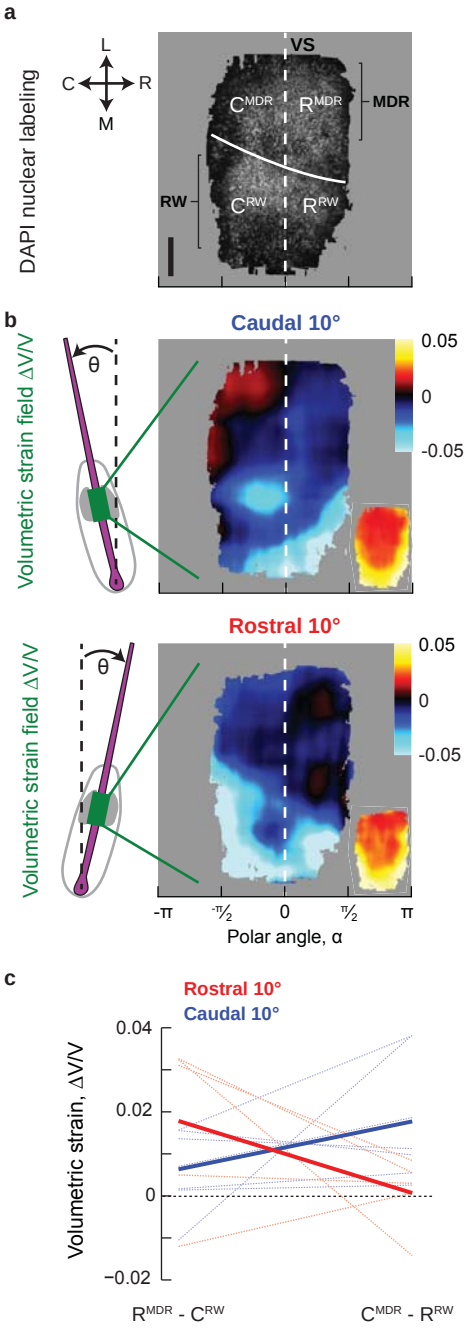


Figure 4r. Whiteley, Knutsen, Matthews & Kleinfeld